Supplementary Information: First-principles-informed energy span and microkinetic analysis of ethanol catalytic conversion to 1,3-butadiene on MgO

Astrid Boje,[a] William E. Taifan,[b] Henrik Ström,[c] Tomáš Bučko,[d,e] Jonas Baltrusaitis,[b] and Anders Hellman*[a,f]

[a] Department of Physics, Chalmers University of Technology, 412 96 Göteborg, Sweden.
[b] Department of Chemical and Biomolecular Engineering, Lehigh University, B336 Iacocca Hall, 111 Research Drive, Bethlehem, PA 18015, USA.
[c] Department of Mechanics and Maritime Sciences, Chalmers University of Technology, 412 96 Göteborg, Sweden.
[d] Department of Physical and Theoretical Chemistry, Faculty of Natural Sciences, Comenius University in Bratislava, Ilkovičova 6, SK-84215, Bratislava, Slovak Republic.
[e] Institute of Inorganic Chemistry, Slovak Academy of Sciences, Dúbravská cesta 9, SK-84236 Bratislava, Slovak Republic.
[f] Competence Centre for Catalysis, Chalmers University of Technology, 412 96 Göteborg, Sweden.
* E-mail: anders.hellman@chalmers.se

Contents

1 Constants

The following values were used in all computations:

- Boltzmann constant: $k_B = 1.380\,662 \times 10^{-23}\,\mathrm{m^2\,kg\,s^{-2}\,K^{-1}}$
- Planck constant: $h = 6.626\,176 \times 10^{-34}\,\mathrm{m^2\,kg\,s^{-1}}$
- Gas constant: $R = 8.314\,462\,62\,\mathrm{J\,mol^{-1}\,K^{-1}}$
- Pressure: $P = 101\,325\,\mathrm{Pa}$.

2 Structures of all surface states

The structures of all surface states used in this work are provided in Table S1. Most structures and energies were taken from the first-principles calculations presented by Taifan *et al.* and more details are given in that study.[1] These states are illustrated here to aid understanding of the steps considered in the current work. Some states were added for this work and these are marked with a dagger (†) throughout the supplementary material. We added transition states for desorption of butadiene from C_4H_6O chemisorbed via the terminal CH_2 and the CH groups (steps 3F–3G and 6G–6H respectively in Taifan *et al.*[1]) and the new transition states are labeled 3Fi and 6Gi. The paths 3F–3Fi–3G and 6G–6Gi–6H are illustrated in Figs. S1 and S2 respectively. They describe similar dissociation processes, with small energetic differences attributable to the specific configuration of atoms on the surface in each state. Other states were included to model hydrogen adsorption (8A–8C), water adsorption and hydroxide dissociation (9A–9D) and acetaldehyde adsorption (10A–10B). Additional activated pathways were included to model possible formation of two further byproducts: butanol from crotyl alcohol (path 3Ci–3Cvi, illustrated in Fig. S3), and ethyl acetate from hemiacetal (path 7Ei–7Eiv, illustrated in Fig. S5).

Table S1 Surface states in all pathways

Ethanol dehydrogenation (path 1)				
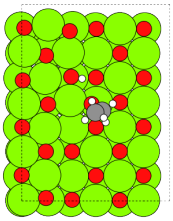	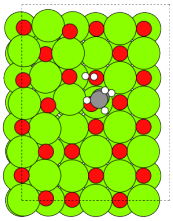	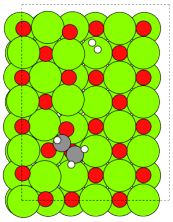		
1A	1B (TS)	1C		
Aldol condensation (path 2)				
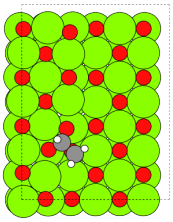	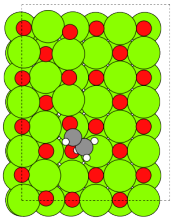	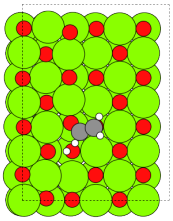	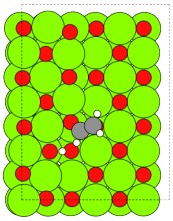	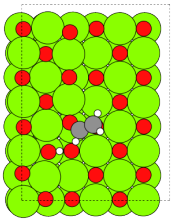
2A	2B (TS)	2C	2D (TS)	2E
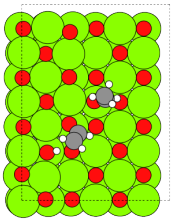	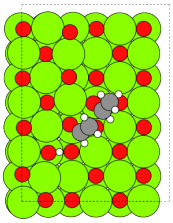	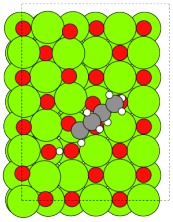	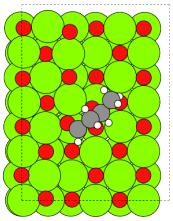	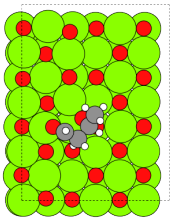
2F	2G (TS)	2H	2I	2J
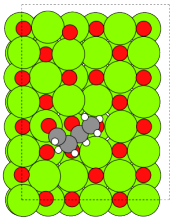	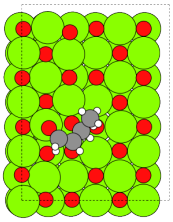	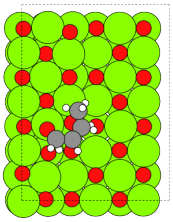	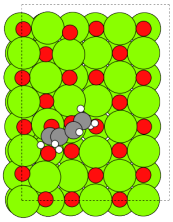	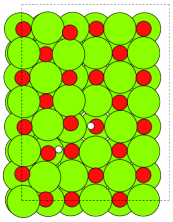
2K (TS)	2L	2M (TS)	2N	2O

MPV reduction – crotonaldehyde (path 3)

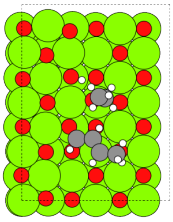
3A

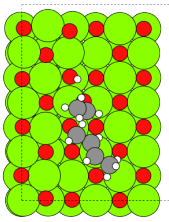
3B (TS)

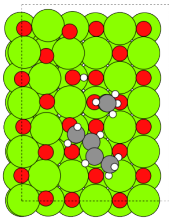
3C

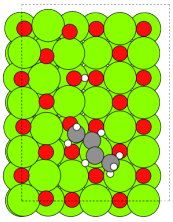
3D

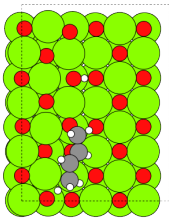
3E (TS)

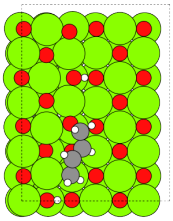
3F

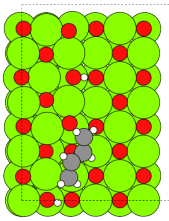
3Fi† (TS)

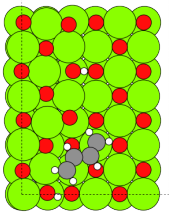
3G

MPV reduction – acetaldol (path 4)

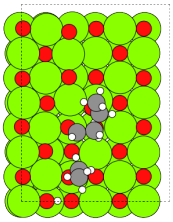
4A

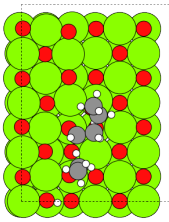
4B (TS)

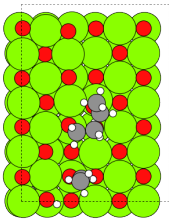
4C

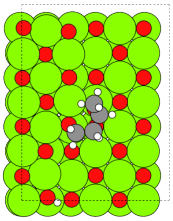
4D

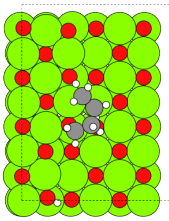
4E (TS)

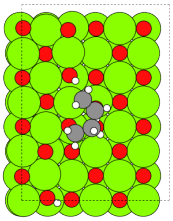
4F

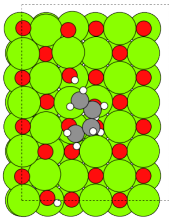
4G (TS)

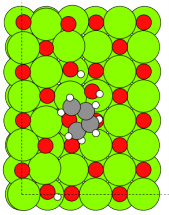
4H

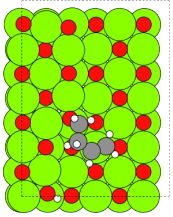
4I

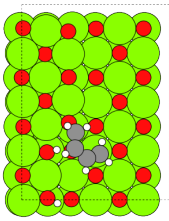
4J (TS)

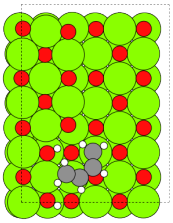
4K

Ethanol dehydration (path 5)

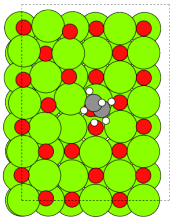
5A

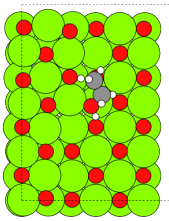
5B (TS)

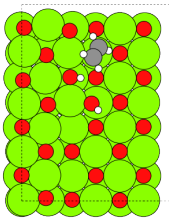
5C

Prins condensation (path 6)

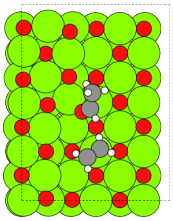
6A

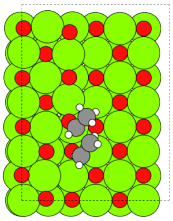
6B (TS)

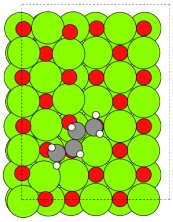
6C

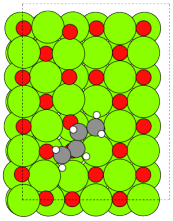
6D (TS)

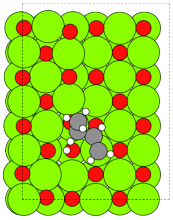
6E

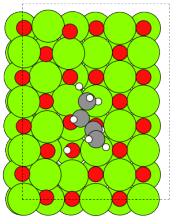
6F (TS)

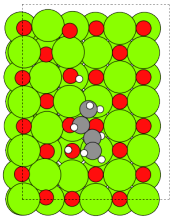
6G

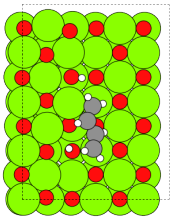
6Gi† (TS)

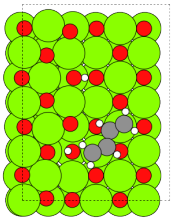
6H

Hemiacetal rearrangement (path 7)

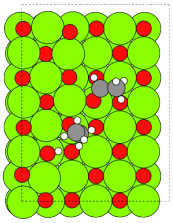
7A

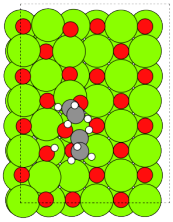
7B (TS)

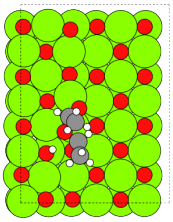
7C

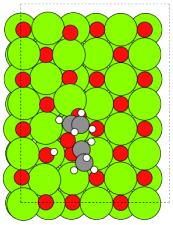
7D (TS)

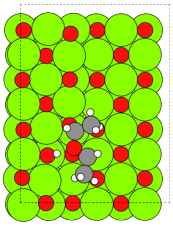
7E

Dissociative hydrogen adsorption (path 8)

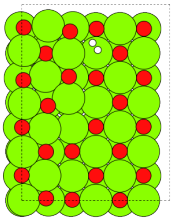
8A†

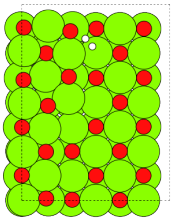
8B† (TS)

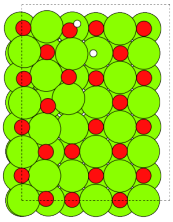
8C†

OH dissociation (path 9)

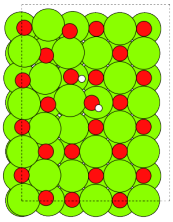
9B†

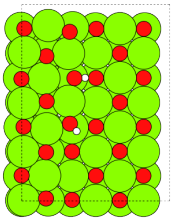
9C†

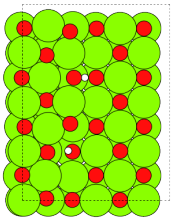
9D†

Acetaldehyde adsorption (path 10)

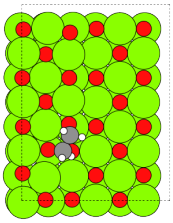

10B†

Butanol from crotyl alkoxide (path 3(b))

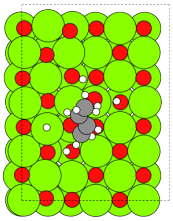

3Ci†

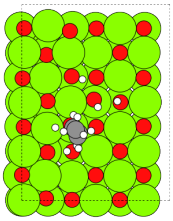

3Cii† (TS)

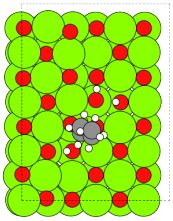

3Ciii†

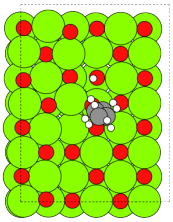

3Civ†

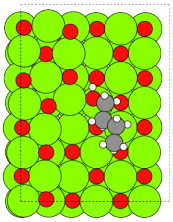

3Cv† (TS)

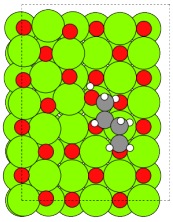

3Cvi†

Ethyl acetate from hemiacetal (path 7(b))

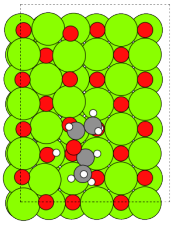

7Ei†

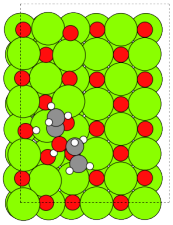

7Eii† (TS)

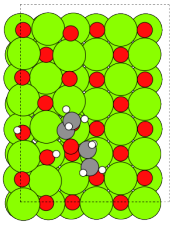

7Eiii†

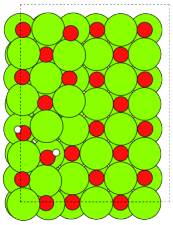

7Eiv†

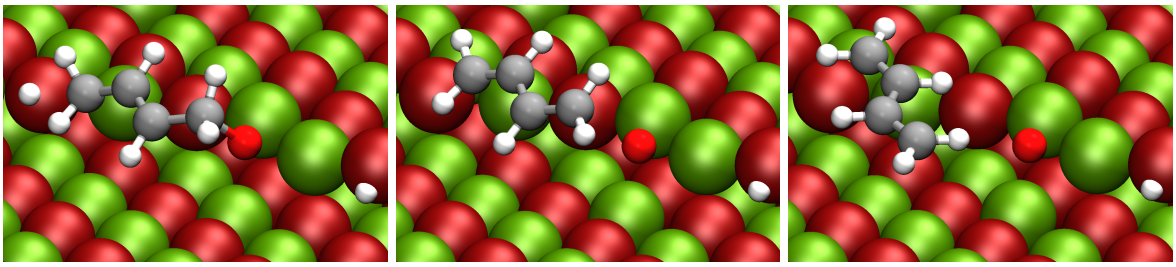

(a) State 3F (b) State 3Fi† (c) State 3G

Fig. S1 Desorption of butadiene chemisorbed via a terminal CH_2 group on the MgO step showing 1(a): initial state, 3F; 1(b): transition state, 3Fi†; and 1(c): final state, 3G.

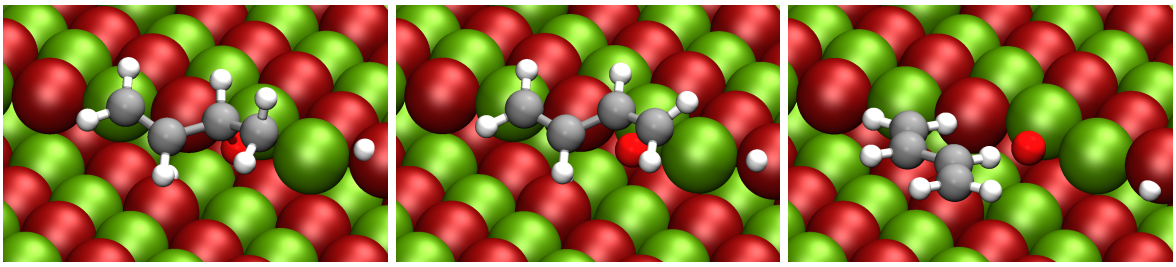

(a) State 6G (b) State 6Gi† (c) State 6H

Fig. S2 Desorption of butadiene chemisorbed via a CH group on the MgO step showing 2(a): initial state, 6G; 2(b): transition state, 6Gi†; and 2(c): final state, 6H.

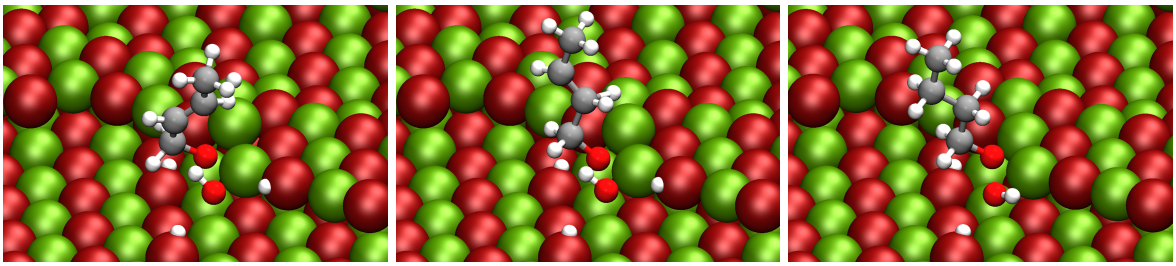

(a) State 3Ci† (b) State 3Cii† (c) State 3Ciii†

Fig. S3 Formation of butoxy from crotyl alkoxide showing 3(a): initial state, 3Ci†; 3(b): transition state, 3Cii†; and 3(c): final state, 3Ciii†.

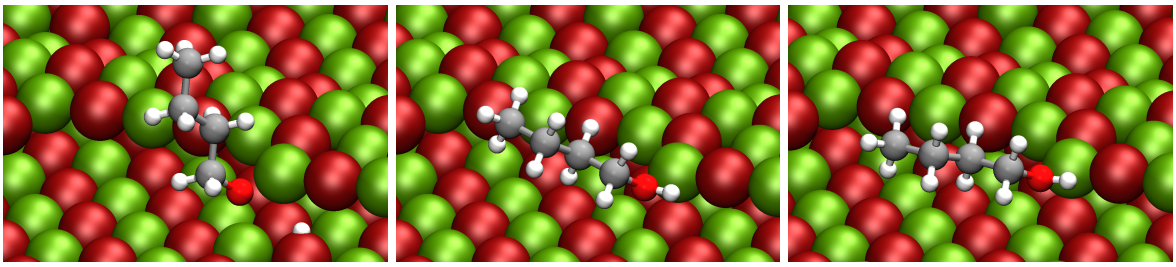

(a) State 3Civ† (b) State 3Cv† (c) State 3Cvi†

Fig. S4 Formation of butanol from butoxy showing 4(a): initial state, 3Civ†; 4(b): transition state, 3Cv†; and 4(c): final state, 3Cvi†.

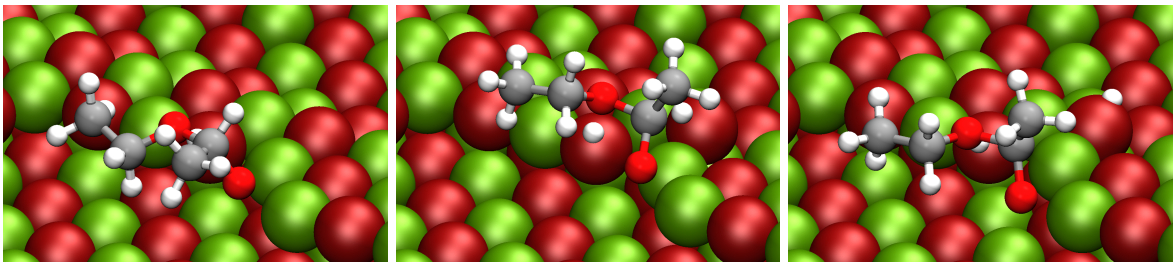

(a) State 7Ei† (b) State 7Eii† (c) State 7Eiii†

Fig. S5 Formation of ethyl acetate from hemiacetal showing 5(a): initial state, 7Ei†; 5(b): transition state, 7Eii†; and 5(c): final state, 7Eiii†.

3 Molecular composition of all states

The surface and gas molecules in each state are listed in Tables S2–S5. Labels I and TS refer to intermediates and transition states, respectively. In the path 4 states of p174, the gas-phase contains one more molecule of ethanol and one fewer molecule of both hydrogen and acetaldehyde.

Table S2 Species in the ethanol dehydrogenation, aldol condensation, and MPV reduction pathways (paths 1–4)

State	I/TS	Surface species	Gas species						
			C_2H_5OH	H_2	H_2O	C_2H_4O	C_4H_6O	$C_4H_{10}O$	$C_4H_8O_2$
0			3	0	0	0	0	0	0
1A	I	C_2H_5O, H	2	0	0	0	0	0	0
1B	TS	C_2H_4O, 2H	2	0	0	0	0	0	0
1C	I	C_2H_4O, H_2	2	0	0	0	0	0	0
2A	I	C_2H_4O	2	1	0	0	0	0	0
2B	TS	C_2H_3O, H	2	1	0	0	0	0	0
2C	I	C_2H_3O, H	2	1	0	0	0	0	0
2D	TS	C_2H_3O, H	2	1	0	0	0	0	0
2E	I	C_2H_3O, H	2	1	0	0	0	0	0
2F	I	C_2H_3O, H, C_2H_4O	1	2	0	0	0	0	0
2G	TS	C_2H_3O, H, C_2H_4O	1	2	0	0	0	0	0
2H	I	$C_4H_7O_2$, H	1	2	0	0	0	0	0
2I	I	$C_4H_8O_2$	1	2	0	0	0	0	0
2J	I	$C_4H_7O_2$, H	1	2	0	0	0	0	0
2K	TS	$C_4H_6O_2$, 2H	1	2	0	0	0	0	0
2L	I	$C_4H_6O_2$, 2H	1	2	0	0	0	0	0
2M	TS	C_4H_6O, 2H, O	1	2	0	0	0	0	0
2N	I	C_4H_6O, 2H, O	1	2	0	0	0	0	0
2O	I	2H, O	1	2	0	0	1	0	0
3A	I	C_4H_6O, C_2H_5O, H	0	2	1	0	0	0	0
3B	TS	C_4H_6O, C_2H_5O, H	0	2	1	0	0	0	0
3C	I	C_4H_7O, C_2H_4O, H	0	2	1	0	0	0	0
3D	I	C_4H_7O, H	0	2	1	1	0	0	0
3E	TS	C_4H_6O, 2H	0	2	1	1	0	0	0
3F	I	C_4H_6O, 2H	0	2	1	1	0	0	0
3Fi†	TS	C_4H_6, 2H, O	0	2	1	1	0	0	0
3G	I	C_4H_6, 2H, O	0	2	1	1	0	0	0
4A	I	$C_4H_7O_2$, C_2H_5O, 2H	0	2	0	0	0	0	0
4B	TS	$C_4H_7O_2$, C_2H_5O, 2H	0	2	0	0	0	0	0
4C	I	$C_4H_8O_2$, C_2H_4O, 2H	0	2	0	0	0	0	0
4C*	I	$C_4H_8O_2$, 2H	0	2	0	1	0	0	0
4D	I	$C_4H_9O_2$, H	0	2	0	1	0	0	0
4E	TS	$C_4H_8O_2$, 2H	0	2	0	1	0	0	0
4F	I	$C_4H_8O_2$, 2H	0	2	0	1	0	0	0
4G	TS	$C_4H_8O_2$, 2H	0	2	0	1	0	0	0
4H	I	C_4H_7O, 2H, OH	0	2	0	1	0	0	0
4I	I	C_4H_7O, H	0	2	1	1	0	0	0
4J	TS	C_4H_6, 2H, O	0	2	1	1	0	0	0
4K	I	C_4H_6, 2H, O	0	2	1	1	0	0	0

Table S3 Species in the ethanol dehydration, Prins condensation, and hemiacetal rearrangement pathways (paths 5–7)

State	I/TS	Surface species	Gas species						
			C_2H_5OH	H_2	H_2O	C_2H_4O	C_4H_6O	$C_4H_{10}O$	$C_4H_8O_2$
5A	I	C_2H_5O, H	2	0	0	0	0	0	0
5B	TS	C_2H_4, OH, H	2	0	0	0	0	0	0
5C	I	C_2H_4, OH, H	2	0	0	0	0	0	0
6A	I	C_2H_4, C_2H_4O	1	1	1	0	0	0	0
6B	TS	C_4H_8O	1	1	1	0	0	0	0
6C	I	C_4H_8O	1	1	1	0	0	0	0
6D	TS	C_4H_7O, H	1	1	1	0	0	0	0
6E	I	C_4H_7O, H	1	1	1	0	0	0	0
6F	TS	C_4H_6O, 2H	1	1	1	0	0	0	0
6G	I	C_4H_6O, 2H	1	1	1	0	0	0	0
6Gi†	TS	C_4H_6, 2H, O	1	1	1	0	0	0	0
6H	I	C_4H_6, 2H, O	1	1	1	0	0	0	0
7A	I	C_2H_4O, C_2H_5O, H	1	1	0	0	0	0	0
7B	TS	C_2H_4O, C_2H_5O, H	1	1	0	0	0	0	0
7C	I	$C_4H_9O_2$, H	1	1	0	0	0	0	0
7D	TS	$C_4H_9O_2$, H	1	1	0	0	0	0	0
7E	I	$C_4H_9O_2$, H	1	1	0	0	0	0	0

Table S4 Species in the adsorption and hydroxide dissociation pathways (paths 8–10)

State	I/TS	Surface species	Gas species						
			C_2H_5OH	H_2	H_2O	C_2H_4O	C_4H_6O	$C_4H_{10}O$	$C_4H_8O_2$
8A†	I	H_2	1	1	0	0	0	0	1
8B†	TS	H, H	1	1	0	0	0	0	1
8C†	I	H, H	1	1	0	0	0	0	1
9A†	I		1	2	1	0	1	0	0
9B†	I	OH, H	1	2	0	0	1	0	0
9C†	I	OH, H	1	2	0	0	1	0	0
9D†	I	O, H, H	1	2	0	0	1	0	0
10A†	I		2	1	0	1	0	0	0
10B†	I	C_2H_4O	2	1	0	0	0	0	0

Table S5 Species in the formation of butanol from crotyl alkoxide (path 3(b)) and ethyl acetate from hemiacetal (path 7(b))

State	I/TS	Surface species	Gas species						
			C_2H_5OH	H_2	H_2O	C_2H_4O	C_4H_6O	$C_4H_{10}O$	$C_4H_8O_2$
3Ci†	I	C_4H_7O, 4H, OH	0	1	0	1	0	0	0
3Cii†	TS	C_4H_8O, 3H, OH	0	1	0	1	0	0	0
3Ciii†	I	C_4H_9O, 2H, OH	0	1	0	1	0	0	0
3Civ†	I	C_4H_9O, H	0	1	1	1	0	0	0
3Cv†	TS	$C_4H_{10}O$	0	1	1	1	0	0	0
3Cvi†	I	$C_4H_{10}O$	0	1	1	1	0	0	0
3Cvii†	I		0	1	1	1	0	1	0
7Ei†	I	$C_4H_9O_2$, H	1	1	0	0	0	0	0
7Eii†	TS	$C_4H_8O_2$, 2H	1	1	0	0	0	0	0
7Eiii†	I	$C_4H_8O_2$, 2H	1	1	0	0	0	0	0
7Eiv†	I	2H	1	1	0	0	0	0	1

4 Energies of states introduced in this work

The relative electronic energies for states introduced in this work (i.e., with compositions in Tables S2–S5) are provided in Table S6. Electronic and total free energies of all states not listed were provided by Taifan *et al.*.[1] The new transition states, 3Fi and 6Gi, yield reaction barriers of $6.8\,\mathrm{kcal\,mol^{-1}}$ and $5.7\,\mathrm{kcal\,mol^{-1}}$ respectively at $723\,\mathrm{K}$. All energies are referenced to the MgO (100) step-edge surface and three gas-phase ethanol molecules. The free energy calculations are described in Section 5.

Table S6 Relative electronic energies at $0\,\mathrm{K}$ and free energies at $723\,\mathrm{K}$.

State	Electronic energy ($\mathrm{kcal\,mol^{-1}}$)	Total free energy ($\mathrm{kcal\,mol^{-1}}$)
	Butadiene desorption with transition states	
3F	8.10	-15.1
3Fi†	15.2	-8.31
3G	7.73	-20.3
6G	-5.72	-0.260
6Gi†	5.05	5.41
6H	-4.09	-2.52
	State 4C excluding acetaldehyde	
4C*	-48.4	-33.7
	Butanol formation from crotyl alkoxide	
3Ci†	3.29	28.7
3Cii†	19.1	45.6
3Ciii†	-57.6	-23.9
3Civ†	-26.7	-22.6
3Cv†	-12.6	-8.69
3Cvi†	-12.6	-9.78
3Cvii†	14.4	-10.0
	Ethyl acetate formation from hemiacetal	
7Ei†	-44.8	-8.14
7Eii†	12.8	48.0
7Eiii†	-6.87	27.5
7Eiv†	32.3	31.7
	Dissociative hydrogen adsorption	
8A†	14.0	9.40
8B†	16.1	16.2
8C†	-7.57	-5.62
	Water adsorption and OH dissociation	
9A†	43.1	-10.5
9B†	1.30	-27.4
9C†	-14.2	-40.7
9D†	9.58	-16.3
	Acetaldehyde adsorption	
10A†	23.1	-5.83
10B†	-20.0	-11.5

5 Free energy calculations

The total free energy, G_{total}, can be approximated by summation of the electronic, translational, vibrational, and rotational contributions as described by Jensen[2] i.e.,

$$G_{\text{total}} = G_{\text{elec}} + G_{\text{tran}} + G_{\text{rota}} + G_{\text{vibr}}. \tag{S1}$$

The electronic contribution, G_{elec}, is taken to be the electronic energy computed by DFT. The translational term is

$$G_{\text{tran}} = -k_{\text{B}}T \ln\left(\frac{V}{N_{\text{A}}}\left(\frac{2\pi M k_{\text{B}}T}{h^2}\right)^{\frac{3}{2}}\right), \tag{S2}$$

where V is the standard molar volume and M is the molecular mass. The rotational term depends on the geometry of the molecule,

$$G_{\text{rota}} = \begin{cases} -k_{\text{B}}T \ln\left(\frac{8\pi^2 k_{\text{B}}TI}{\sigma h^2}\right) & \text{linear molecule} \\ -k_{\text{B}}T \ln\left(\frac{\sqrt{\pi}}{\sigma}\left(\frac{8\pi^2 k_{\text{B}}T}{h^2}\right)^{\frac{3}{2}}\sqrt{I_1 I_2 I_3}\right) & \text{otherwise.} \end{cases} \tag{S3}$$

Here, I and I_1, I_2, I_3 are the inertia and three principle components of the inertia, respectively. The symmetry numbers, σ, for relevant species are provided in Table S7.

Table S7 Symmetry indices used to compute rotational energy terms for gas molecules

Species	Value
Acetaldehyde	1
Butadiene	2
Crotonaldehyde	1
Ethanol	1
Hydrogen	2
Water	2
Butanol	1
Ethyl acetate	1

The vibrational term is computed by summation of the vibrational frequencies, ν_i, accounting for all degrees of freedom (DOF) not attributed to overall translational or rotational movement.

$$G_{\text{vibr}} = k_{\text{B}} \sum_{i=1}^{N_{\text{dof}}} \left[\frac{h\nu_i}{2k_{\text{B}}} + T \ln\left(1 - e^{-\frac{h\nu_i}{k_{\text{B}}T}}\right)\right]. \tag{S4}$$

For transition states, one of the vibrational frequencies is formally imaginary,[2] resulting in one fewer vibrational degrees of freedom. Here, as in Taifan *et al.*,[1] it is assumed that molecules interacting with the surface experience no translational or rotational contributions and that molecules in the gas-phase have three translational and two/three rotational contributions for linear/nonlinear molecules respectively. The number of atoms considered includes all surface atoms, N_{s}, except the immobile bottom layer, and all atoms in the molecules interacting with the surface, N_{m}, or all atoms for freely moving gases, N_{g}. Thus, for each constituent, the number of degrees of freedom:

$$N_{\text{dof}} = \begin{cases} 3N_{\text{s}} & \text{Clean surface} \\ 3N_{\text{s}} + 3N_{\text{m}} & \text{Surface-bound state} \\ 3N_{\text{g}} - 5/6 & \text{Linear/nonlinear gas molecule.} \end{cases} \tag{S5}$$

The free energy contributions arising from translational, rotational and vibrational degrees of freedom are all affected by temperature as shown in Eqs. S2–S4. This has a varied impact on the relative free energies of different states as

illustrated in Fig. S6 for several states.

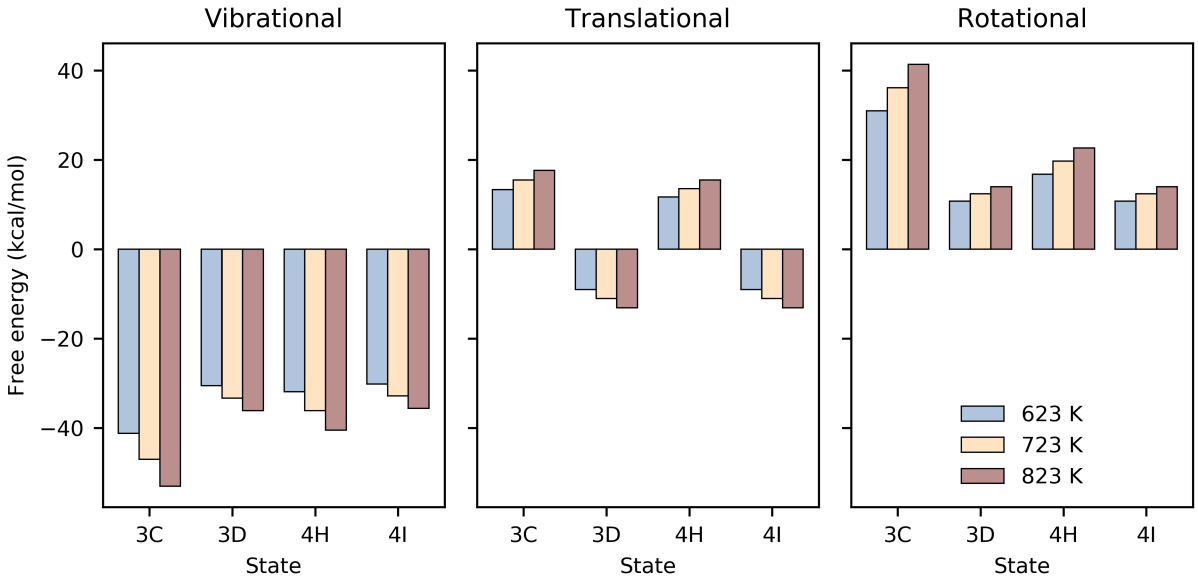

Fig. S6 Free energy contributions arising from vibrational, translational, and rotational degrees of freedom of select states as a function of temperature. Surface bound molecules only contribute to the vibrational component, while gas molecules have vibrational, translational, and rotational components. Values are relative to the respective free energy contributions of the reference state.

The forward and reverse reaction barriers were computed as the difference in Gibbs free energy between the transition state (TS) and initial state (IS) for the forward reaction,

$$\Delta G_{\mathrm{a}}^{\mathrm{f}} = G_{\mathrm{total,TS}} - G_{\mathrm{total,IS}}, \tag{S6}$$

and the transition state and the final state (FS) for the reverse reaction,

$$\Delta G_{\mathrm{a}}^{\mathrm{r}} = G_{\mathrm{total,TS}} - G_{\mathrm{total,FS}}, \tag{S7}$$

respectively. The reaction energies were computed as the difference in Gibbs free energy between each pair of initial and final states,

$$\Delta G_{\mathrm{r}} = G_{\mathrm{total,FS}} - G_{\mathrm{total,IS}}. \tag{S8}$$

The reaction barriers and energies for all steps modeled in this work are given in Table S8 for three representative temperatures: 623 K, 723 K, and 823 K.

Table S8 Reaction forward and reverse barriers and reaction energies for steps modeled in this work.

Path	ΔG_a^f (kcal mol^{-1})			ΔG_a^r (kcal mol^{-1})			ΔG_r (kcal mol^{-1})		
	623 K	723 K	823 K	623 K	723 K	823 K	623 K	723 K	823 K
1A–C	39.6	39.6	39.7	20.0	20.2	20.5	19.6	19.4	19.2
2A–C	15.8	15.9	16.1	27.1	27.7	28.4	-11.3	-11.8	-12.3
2F–H	14.6	16.1	17.6	3.05	3.21	3.40	11.5	12.9	14.2
2J–L	5.22	5.80	6.39	11.5	12.4	13.3	-6.27	-6.60	-6.94
2L–N	23.7	23.8	23.9	11.5	12.4	13.4	12.2	11.3	10.5
2N–O	0	0	0	0	0	0	-18.8	-22.1	-25.3
3A–C	11.5	12.3	13.0	7.74	8.58	9.44	3.79	3.69	3.60
3D–F	26.8	27.6	28.4	14.4	15.0	15.7	12.4	12.5	12.7
†3F–G	6.67	6.75	6.86	11.1	12.0	12.8	-4.48	-5.22	-5.97
4A–C	8.16	9.76	11.4	16.2	17.3	18.5	-8.03	-7.57	-7.10
4C*–D	0	0	0	0	0	0	1.97	1.77	1.57
4D–F	25.7	26.2	26.8	2.11	2.49	2.89	23.6	23.7	23.9
4F–H	2.02	2.18	2.35	38.7	40.1	41.6	-36.7	-37.9	-39.2
4I–K	32.1	32.5	32.8	17.8	18.8	19.9	14.3	13.7	13.0
5A–C	33.4	33.4	33.3	36.5	38.3	40.0	-3.10	-4.89	-6.72
6A–C	26.3	28.6	30.9	52.1	51.2	50.3	-25.8	-22.6	-19.4
6C–E	38.2	38.7	39.2	33.6	34.6	35.7	4.57	4.06	3.54
6E–G	33.8	34.1	34.4	15.3	15.9	16.4	18.5	18.2	17.9
†6G–H	6.24	5.67	5.13	7.90	7.94	7.99	-1.66	-2.26	-2.86
7A–E	31.1	32.9	34.7	14.8	15.1	15.4	16.3	17.8	19.3
0–1A	0	0	0	0	0	0	-16.9	-13.4	-9.98
†8A–C	5.79	6.77	7.80	21.6	21.8	22.0	-15.8	-15.0	-14.2
†9A–B	0	0	0	0	0	0	-20.0	-16.9	-13.8
†9C–D	0	0	0	0	0	0	24.3	24.4	24.6
†10A–B	0	0	0	0	0	0	-10.4	-5.66	-0.938
†3Ci–iii	16.5	16.9	17.3	69.8	69.5	69.2	-53.3	-52.6	-51.9
†3Civ–vi	13.9	14.0	14.1	0.758	1.09	1.45	13.1	12.9	12.6
†3Cvi–vii	0	0	0	0	0	0	3.01	-0.237	-3.41
†7Ei–iii	55.8	56.1	56.5	19.9	20.5	21.0	35.9	35.7	35.5
†7Eiii–iv	0	0	0	0	0	0	8.67	4.21	-0.168

6 Energy span model

We used the energy span model of Kozuch and Shaik[3] to predict the TOF and distribution of TOF control between the intermediates and transition states in the mechanism, according to the free energy landscapes of each pathway. As a reminder, the pathways include (Fig. 1 in the main text): ethanol dehydrogenation and aldol condensation with MPV reduction from crotonaldehyde (p123); ethanol dehydrogenation and aldol condensation with MPV reduction from 3-hydroxybutanal (p124); ethanol dehydration and Prins condensation (p156); and ethanol dehydrogenation with nucleophillic addition and rearrangement (p174). The free energy landscapes for p123, p124 and p156 are provided in the main text (Fig. 2, panels (a)–(c)) and that of p174 is provided here (Fig. S7, panel (a)). Increasing the temperature from 723 K to 823 K raises the free energy profile for p174 and reducing the temperature to 623 K has the opposite effect. As discussed in the main text, intermediate 4H and transition state 1B are strongly TOF-controlling for p174 at all three temperatures (Fig. S7, panels (b) and (c) respectively). The energy span approximation finds the largest energy difference between a stable intermediate and hard-to-reach transition state, across catalytic cycles. This can be illustrates graphically on the free energy landscape, as shown in Figs. S8–S11. The TDTS comes before the TDI in pathways 124, 156 and 174; thus, the reaction energy must be included when measuring the energy span. In the case of p156, both transition states 5B and 6B show significant degrees of TOF control so there is more than one important transition state in the energy landscape for this pathway and the energy span approximation is not expected to predict the TOF correctly.

For p123, the TDI is state 2E and the TDTS is state 2M. The energy span is $43.6\,\mathrm{kcal\,mol^{-1}}$ at 723 K (Fig. S8). For p124, the TDI is state 4H and the TDTS is state 1B – which occurs in the previous cycle (shaded zone spans two cycles in Fig. S9). Thus, the reaction energy of $-23.8\,\mathrm{kcal\,mol^{-1}}$ must be included, yielding an energy span of $48.4\,\mathrm{kcal\,mol^{-1}}$. The situation for p174 is similar (Fig. S11), but in this case, the reaction 1A–1C is followed by state 1A again, obtaining adsorbed ethanol and acetaldehyde as state 7A. Here, state 7E ($C_4H_9O_2$) is taken to be followed directly by state 4E ($C_4H_8O_2$ and H), ignoring the different structures of $C_4H_9O_2$ present in states 7E and 4D. Thus, the TOF may be overestimated for p174. The rate-determining intermediate and transition state are as in p124; thus, the energy span is also the same. Finally, in p156, there are two transition states with similar free energies at 723 K (Fig. S10). The energy span is computed between intermediate state 6C and transition state 5B, across the catalytic cycle, and includes the relatively small reaction driving force of $-2.51\,\mathrm{kcal\,mol^{-1}}$, yielding a span of $49.0\,\mathrm{kcal\,mol^{-1}}$.

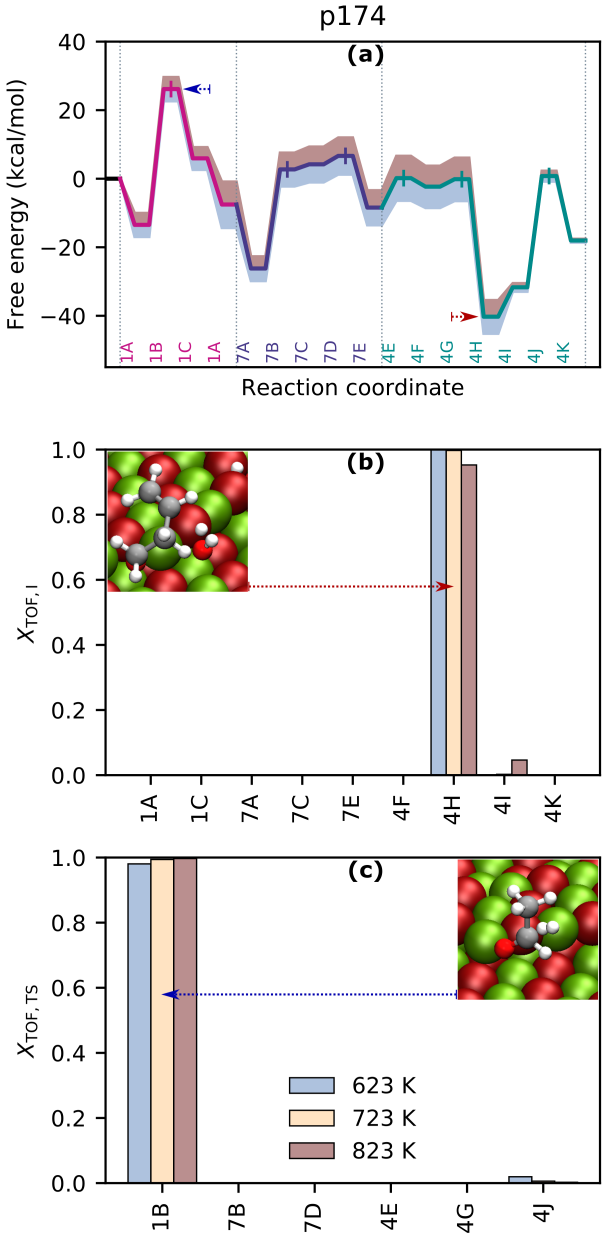

Fig. S7 Free energy landscape for pathway 174 and its rate controlling states. Panel (a): Free energy landscape at 723 K. Transition states labeled with + symbols. Effect of increasing (red) and decreasing (blue) temperature by 100 K indicated by filled regions. Molecules associated with each state are as in Taifan *et al.*[1]. TDI and TDTS marked with red and blue dashed arrows. Panels (b) and (c): Energy span assessment of relative TOF contributions of intermediates and transition states with insets showing states with maximum contributions.

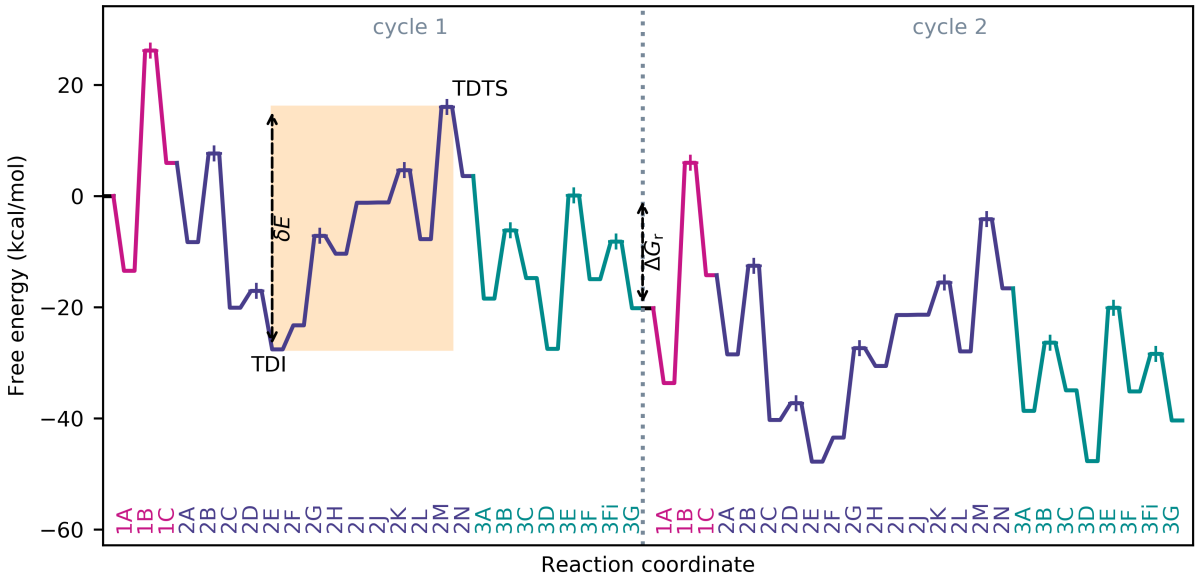

Fig. S8 Graphical energy span analysis for pathway 123 at 723 K. Dashed vertical arrows indicate reaction energy, ΔG_r, of one cycle and energy span, δE, for TOF-determining transition state (TDTS) and intermediate (TDI). Transition states marked with + symbols.

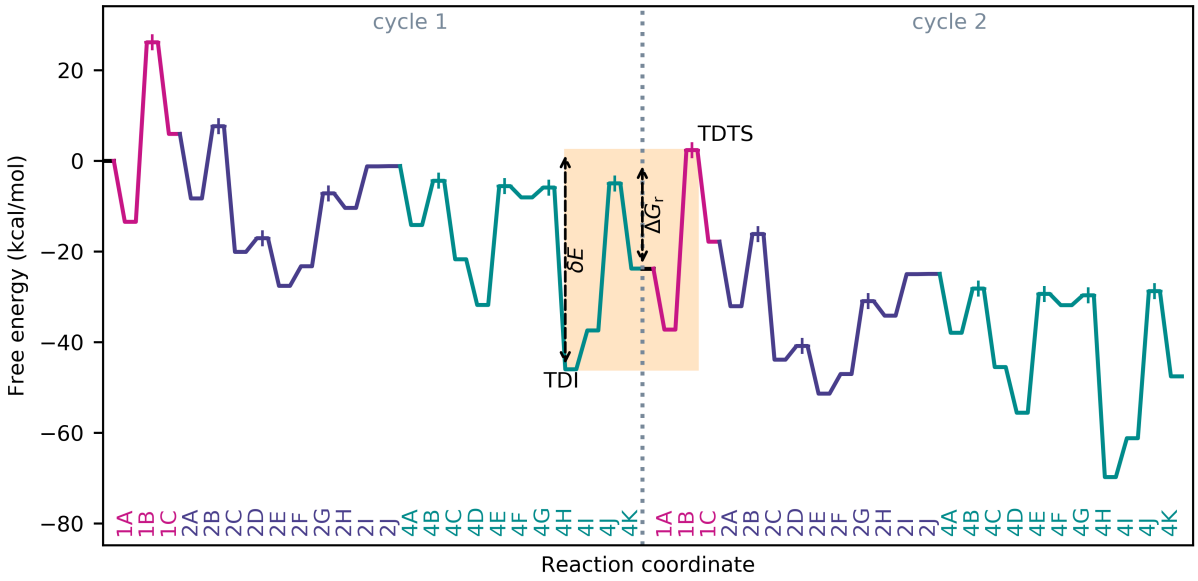

Fig. S9 Graphical energy span analysis for pathway p124 at 723 K. Dashed vertical arrows indicate reaction energy, ΔG_r, of one cycle and energy span, δE, for TOF-determining transition state (TDTS) and intermediate (TDI). Transition states marked with + symbols.

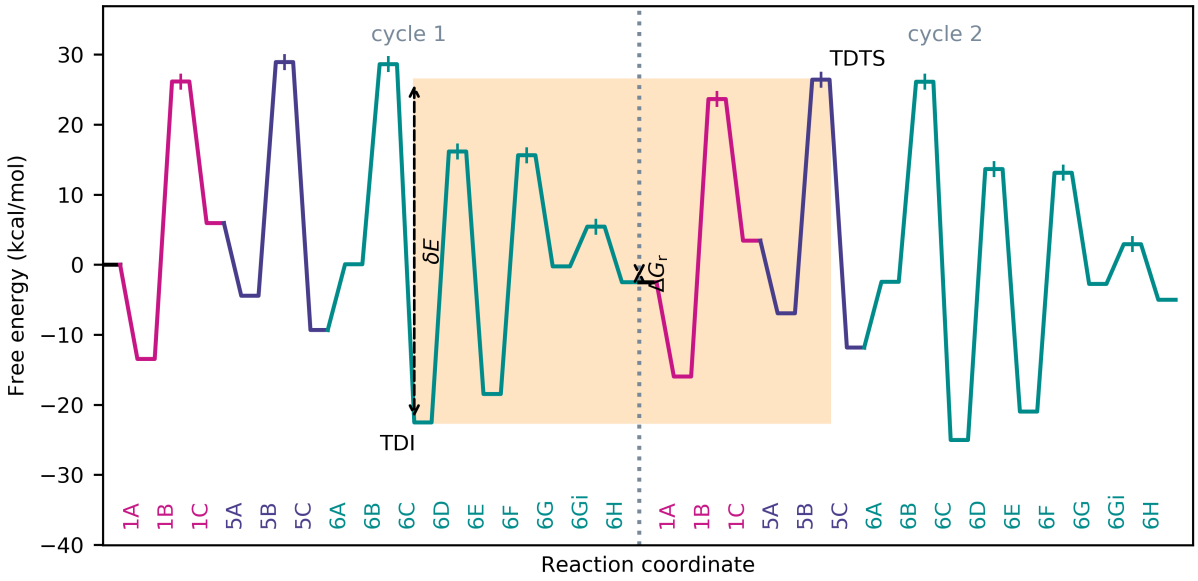

Fig. S10 Graphical energy span analysis for pathway 156 at 723 K. Dashed vertical arrows indicate reaction energy, ΔG_r, of one cycle and energy span, δE, for TOF-determining transition state (TDTS) and intermediate (TDI). Transition states marked with + symbols.

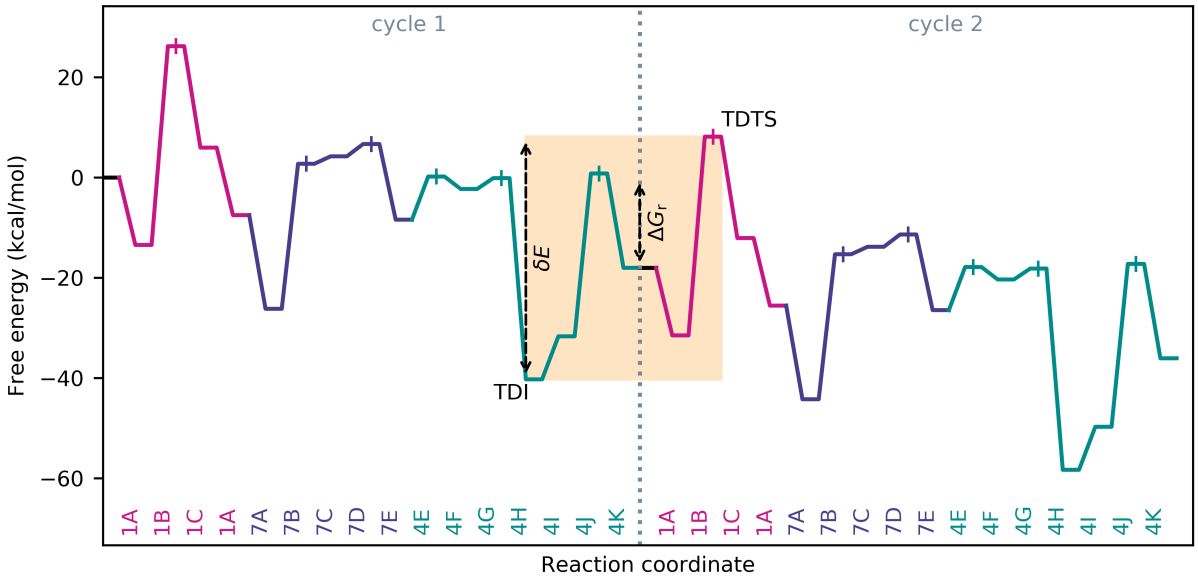

Fig. S11 Graphical energy span analysis for pathway 174 at 723 K. Dashed vertical arrows indicate reaction energy, ΔG_r, of one cycle and energy span, δE, for TOF-determining transition state (TDTS) and intermediate (TDI). Transition states marked with + symbols.

7 Microkinetic model

A microkinetic model was formulated based on the pathways proposed by Taifan and coworkers[1] and implemented using the Python Catalysis Kinetics (PyCatKin) toolset.[4] The reaction steps and net rates are formulated in Table S9. Here, θ represents the fraction of sites occupied by the sub-scripted adsorbate (i.e., the surface coverage), and θ_* represents the fraction of unoccupied/free sites,

$$\theta_* = 1 - \sum_{\text{adsorbates}} \theta_{\text{adsorbate}}.$$

The forward and reverse rate constants are given by k^{f} and k^{r}, respectively, and r is the net reaction rate. Superscripts i are used to distinguish different structures with the same chemical formula, which are modeled as distinct species. The differential equations describing the change in surface coverage of each species are listed in Table S11. These were solved in Python, using the SciPy ODE solver *solve_ivp* with the implicit, multi-step, variable-order, backwards difference formula (BDF) method,[5] and relative and absolute tolerances of 10^{-6} and 10^{-8}, respectively. An analytic expression was derived for the Jacobian and provided to the solver. The steady-state values, θ^{ss}, were obtained by solving the equations in Table S11 for zero using the SciPy *least_squares* minimizer with the Trust Region Reflective method,[6] a function tolerance of 10^{-8}, and a maximum of 10^4 function evaluations. The objective (cost) function is given by the sum of squares of the ODEs,

$$\min_{\theta} f(\theta) = \min_{\{\theta_{\text{adsorbate}}\}} \sum_{\text{adsorbates}} \left(\frac{d\theta_{\text{adsorbate}}}{dt} \right)^2.$$

The final time values, $\theta_{\text{adsorbate}}(t_{\text{f}})$, were used as the initial guess, and the solver tolerance was set to 10^{-6}. The values at the final time were compared with the steady-state values using the Euclidean norm:

$$d^{\text{ss}} = \sqrt{\sum_{\text{adsorbates}} \left(\theta_{\text{adsorbate}}(t_{\text{f}}) - \theta^{\text{ss}}_{\text{adsorbate}} \right)^2}.$$

The objective function values at the obtained steady-states are listed in Table S12, along with the distance to steady-state, d^{ss}, at the final time. The convergence to steady-state in the TOF of butadiene formation is studied in Fig. S12. This analysis demonstrates that the gradients in the solutions are satisfactorily small after 24 h at all temperatures in the range 523 K–623 K; thus, this is taken as the final time in all subsequent simulations. As this study did not consider mass transport, there is no retention time to account for in the model and the partial pressures in the gas-phase are fixed. Figs. S13–S15 show the transient surface coverage of the dominant adsorbates (i.e., species occupying at least 2% of the surface sites) for each pathway (p123, p124 and p156) modeled in isolation. The coverage obtained for each pathway in isolation shows high overall surface occupancy with only a few (2–4) significant adsorbates corresponding to stable intermediates along each pathway.

Butadiene selectivity is mapped as a function of temperature and ethanol partial pressure in the main text. The carbon-containing byproducts modeled in the butadiene mechanism include ethylene, acetaldehyde and crotonaldehyde, and their selectivities are compared in Fig. S16, which shows mostly acetaldehyde formation with less than 1 % crotonaldehyde under all conditions, and a few percent ethylene at temperatures above 800 K. Experimental and theoretical observations of ethanol conversion on pure MgO suggest that other byproducts, especially butanol, should be expected.[7–9] To investigate this further, we expanded the model to consider formation of butanol from crotyl alkoxide (state 3C) and ethyl acetate from hemiacetal (state 7E). For butanol, we considered both a double protonation step to saturate the carbons (3Ci–iii) followed by protonation of the resulting butoxy (3Civ–vi) and desorption (3Cvi–vii) with energies calculated in this work, and successive hydrogen transfer from the surface (S10 and S13 in Table S10) and migration (S12) to saturate the carbons in crotyl alkoxide, followed by protonation of the resulting butoxy and desorption (S24) using the free energies calculated by Souza *et al.*[10] in their DFT study of butanol formation on MgO. For ethyl acetate, we considered deprotonation of hemiacetal (7Ei–iii) and desorption (7Eiii–iv) with energies calculated in this work. The additional steps are provided in Table S10. The additional steps were not found to significantly alter the butadiene TOF (Fig. S17) or selectivity because neither butanol nor ethyl acetate was formed to a large extent due to low favorability of the required intermediates in both cases. In particular, lack of crotyl alkoxide due to more preferential desorption of crotonaldehyde than reduction by ethoxide is the reason for both the low rate of formation of butanol and the low activity of p123 in the butadiene model.

Table S9 Forward and reverse reaction steps and rate equations

	Path	Reaction	Net rate
1	1A–C	$C_2H_5O + H \leftrightarrow C_2H_4O + H_{2(g)}$	$r_1 = k_1^f \theta_{C_2H_5O} \theta_H - k_1^r p_{H_2} \theta_{C_2H_4O} \theta_*$
2	2A–C	$C_2H_4O \leftrightarrow C_2H_3O + H$	$r_2 = k_2^f \theta_{C_2H_4O} \theta_* - k_2^r \theta_{C_2H_3O} \theta_H$
3	2F–H	$C_2H_3O + C_2H_4O \leftrightarrow C_4H_7O_2$	$r_3 = k_3^f \theta_{C_2H_3O} \theta_{C_2H_4O} - k_3^r \theta_{C_4H_7O_2} \theta_*$
4	2J–L	$C_4H_7O_2 \leftrightarrow C_4H_6O_2 + H$	$r_4 = k_4^f \theta_{C_4H_7O_2} \theta_* - k_4^r \theta_{C_4H_6O_2} \theta_H$
5	2L–N	$C_4H_6O_2 \leftrightarrow C_4H_6O^{i_1} + O$	$r_5 = k_5^f \theta_{C_4H_6O_2} \theta_* - k_5^r \theta_{C_4H_6O^{i_1}} \theta_O$
6	3A–C	$C_2H_5O + C_4H_6O^{i_1} \leftrightarrow C_2H_4O + C_4H_7O^{i_1}$	$r_6 = k_6^f \theta_{C_2H_5O} \theta_{C_4H_6O^{i_1}} - k_6^r \theta_{C_2H_4O} \theta_{C_4H_7O^{i_1}}$
7	3D–F	$C_4H_7O^{i_1} \leftrightarrow C_4H_6O^{i_2} + H$	$r_7 = k_7^f \theta_{C_4H_7O^{i_1}} \theta_* - k_7^r \theta_{C_4H_6O^{i_2}} \theta_H$
8	3F–G	$C_4H_6O^{i_2} \leftrightarrow O + C_4H_{6(g)}$	$r_8 = k_8^f \theta_{C_4H_6O^{i_2}} - k_8^r p_{C_4H_6} \theta_O$
9	4A–C	$C_2H_5O + C_4H_7O_2 \leftrightarrow C_2H_4O + C_4H_8O_2{}^{i_1}$	$r_9 = k_9^f \theta_{C_2H_5O} \theta_{C_4H_7O_2} - k_9^r \theta_{C_2H_4O} \theta_{C_4H_8O_2{}^{i_1}}$
10	4C*–D	$C_4H_8O_2{}^{i_1} + H \leftrightarrow C_4H_9O_2{}^{i_1}$	$r_{10} = k_{10}^f \theta_{C_4H_8O_2{}^{i_1}} \theta_H - k_{10}^r \theta_{C_4H_9O_2{}^{i_1}} \theta_*$
11	4D–F	$C_4H_9O_2{}^{i_1} \leftrightarrow C_4H_8O_2{}^{i_2} + H$	$r_{11} = k_{11}^f \theta_{C_4H_9O_2{}^{i_1}} \theta_* - k_{11}^r \theta_{C_4H_8O_2{}^{i_2}} \theta_H$
12	4F–H	$C_4H_8O_2{}^{i_2} \leftrightarrow C_4H_7O^{i_2} + OH$	$r_{12} = k_{12}^f \theta_{C_4H_8O_2{}^{i_2}} \theta_* - k_{12}^r \theta_{C_4H_7O^{i_2}} \theta_{OH}$
13	4I–K	$C_4H_7O^{i_2} \leftrightarrow O + H + C_4H_{6(g)}$	$r_{13} = k_{13}^f \theta_{C_4H_7O^{i_2}} \theta_* - k_{13}^r p_{C_4H_6} \theta_O \theta_H$
14	5A–C	$C_2H_5O + H \leftrightarrow OH + H + C_2H_{4(g)}$	$r_{14} = k_{14}^f \theta_{C_2H_5O} \theta_H - k_{14}^r p_{C_2H_4} \theta_{OH} \theta_H$
15	6A–C	$C_2H_4O + C_2H_{4(g)} \leftrightarrow C_4H_8O$	$r_{15} = k_{15}^f p_{C_2H_4} \theta_{C_2H_4O} \theta_* - k_{15}^r \theta_{C_4H_8O} \theta_*$
16	6C–E	$C_4H_8O \leftrightarrow C_4H_7O^{i_3} + H$	$r_{16} = k_{16}^f \theta_{C_4H_8O} \theta_* - k_{16}^r \theta_{C_4H_7O^{i_3}} \theta_H$
17	6E–G	$C_4H_7O^{i_3} \leftrightarrow C_4H_6O^{i_3} + H$	$r_{17} = k_{17}^f \theta_{C_4H_7O^{i_3}} \theta_* - k_{17}^r \theta_{C_4H_6O^{i_3}} \theta_H$
18	6G–H	$C_4H_6O^{i_3} \leftrightarrow O + C_4H_{6(g)}$	$r_{18} = k_{18}^f \theta_{C_4H_6O^{i_3}} - k_{18}^r p_{C_4H_6} \theta_O$
19	7A–E	$C_2H_4O + C_2H_5O \leftrightarrow C_4H_9O_2{}^{i_2}$	$r_{19} = k_{19}^f \theta_{C_2H_4O} \theta_{C_2H_5O} - k_{19}^r \theta_{C_4H_9O_2{}^{i_2}} \theta_*$
20	9C–D	$OH \leftrightarrow H + O$	$r_{20} = k_{20}^f \theta_{OH} \theta_* - k_{20}^r \theta_H \theta_O$
21	0–1A	$C_2H_5OH_{(g)} \leftrightarrow C_2H_5O + H$	$r_{21} = k_{21}^f p_{C_2H_5OH} \theta_*^2 - k_{21}^r \theta_{C_2H_5O} \theta_H$
22	8A–C	$H_{2(g)} \leftrightarrow 2H$	$r_{22} = k_{22}^f p_{H_2} \theta_*^2 - k_{22}^r \theta_H^2$
23	9A–B	$H_2O_{(g)} \leftrightarrow OH + H$	$r_{23} = k_{23}^f p_{H_2O} \theta_*^2 - k_{23}^r \theta_{OH} \theta_H$
24	10A–B	$C_2H_4O_{(g)} \leftrightarrow C_2H_4O$	$r_{24} = k_{24}^f p_{C_2H_4O} \theta_* - k_{24}^r \theta_{C_2H_4O}$
25	2O–N	$C_4H_6O_{(g)} \leftrightarrow C_4H_6O^{i_1}$	$r_{25} = k_{25}^f p_{C_4H_6O} \theta_* - k_{25}^r \theta_{C_4H_6O^{i_1}}$

Table S10 Additional forward and reverse reaction steps and rate equations considered to model byproduct formation

	Path	Reaction	Net rate
26	S10	$C_4H_7O^{i_1} + H \leftrightarrow C_4H_8O^{i_2}$	$r_{26} = k_{26}^f \theta_{C_4H_7O^{i_1}} \theta_H - k_{26}^r \theta_{C_4H_8O^{i_2}} \theta_*$
27	S12	$C_4H_8O^{i_2} \leftrightarrow C_4H_8O^{i_3}$	$r_{27} = k_{27}^f \theta_{C_4H_8O^{i_2}} - k_{27}^r \theta_{C_4H_8O^{i_3}}$
28	S13	$C_4H_8O^{i_3} + H \leftrightarrow C_4H_9O$	$r_{28} = k_{28}^f \theta_{C_4H_8O^{i_3}} \theta_H - k_{28}^r \theta_{C_4H_9O} \theta_*$
29	S24	$C_4H_9O + H \leftrightarrow C_4H_{10}O_{(g)}$	$r_{29} = k_{29}^f \theta_{C_4H_9O} \theta_H - k_{29}^r p_{C_4H_{10}O} \theta_*^2$
30	3Ci–iii	$C_4H_7O^{i_1} + 2H \leftrightarrow C_4H_9O$	$r_{30} = k_{30}^f \theta_{C_4H_7O^{i_1}} \theta_H^2 - k_{30}^r \theta_{C_4H_9O} \theta_*^2$
31	3Civ–vi	$C_4H_9O + H \leftrightarrow C_4H_{10}O$	$r_{31} = k_{31}^f \theta_{C_4H_9O} \theta_H - k_{31}^r \theta_{C_4H_{10}O} \theta_*$
32	3Cvi–vii	$C_4H_{10}O \leftrightarrow C_4H_{10}O_{(g)}$	$r_{32} = k_{32}^f \theta_{C_4H_{10}O} - k_{32}^r p_{C_4H_{10}O} \theta_*$
33	7Ei–iii	$C_4H_9O_2{}^{i_2} \leftrightarrow C_4H_8O_2{}^{i_3} + H$	$r_{33} = k_{33}^f \theta_{C_4H_9O_2{}^{i_2}} \theta_* - k_{33}^r \theta_{C_4H_8O_2{}^{i_3}} \theta_H$
34	7Eiii–iv	$C_4H_8O_2{}^{i_3} \leftrightarrow C_4H_8O_{2(g)}$	$r_{34} = k_{34}^f \theta_{C_4H_8O_2{}^{i_3}} - k_{34}^r p_{C_4H_8O_2} \theta_*$

Table S11 Species coverage equations from rates in Table S9

Species	Production rate
H	$\frac{d\theta_{H}}{dt} = -r_1 + r_2 + r_4 + r_7 - r_{10} + r_{11} + r_{13} + r_{16} + r_{17} + r_{20} + r_{21} + 2r_{22} + r_{23}$
O	$\frac{d\theta_{O}}{dt} = r_5 + r_8 + r_{13} + r_{18} + r_{20}$
OH	$\frac{d\theta_{OH}}{dt} = r_{12} + r_{14} - r_{20} + r_{23}$
C_2H_3O	$\frac{d\theta_{C_2H_3O}}{dt} = r_2 - r_3$
C_2H_4O	$\frac{d\theta_{C_2H_4O}}{dt} = r_1 - r_2 - r_3 + r_6 + r_9 - r_{15} - r_{19} + r_{24}$
C_2H_5O	$\frac{d\theta_{C_2H_5O}}{dt} = -r_1 - r_6 - r_9 - r_{14} - r_{19} + r_{21}$
$C_4H_6O^{i_1}$	$\frac{d\theta_{C_4H_6O^{i_1}}}{dt} = r_5 - r_6 + r_{25}$
$C_4H_6O^{i_2}$	$\frac{d\theta_{C_4H_6O^{i_2}}}{dt} = r_7 - r_8$
$C_4H_6O^{i_3}$	$\frac{d\theta_{C_4H_6O^{i_3}}}{dt} = r_{17} - r_{18}$
$C_4H_7O^{i_1}$	$\frac{d\theta_{C_4H_7O^{i_1}}}{dt} = r_6 - r_7$
$C_4H_7O^{i_2}$	$\frac{d\theta_{C_4H_7O^{i_2}}}{dt} = r_{12} - r_{13}$
$C_4H_7O^{i_3}$	$\frac{d\theta_{C_4H_7O^{i_3}}}{dt} = r_{16} - r_{17}$
C_4H_8O	$\frac{d\theta_{C_4H_8O}}{dt} = r_{15} - r_{16}$
$C_4H_6O_2$	$\frac{d\theta_{C_4H_6O_2}}{dt} = r_4 - r_5$
$C_4H_7O_2$	$\frac{d\theta_{C_4H_7O_2}}{dt} = r_3 - r_4 - r_9$
$C_4H_8O_2{}^{i_1}$	$\frac{d\theta_{C_4H_8O_2{}^{i_1}}}{dt} = r_9 - r_{10}$
$C_4H_8O_2{}^{i_2}$	$\frac{d\theta_{C_4H_8O_2{}^{i_2}}}{dt} = r_{11} - r_{12}$
$C_4H_9O_2{}^{i_1}$	$\frac{d\theta_{C_4H_9O_2{}^{i_1}}}{dt} = r_{10} - r_{11}$
$C_4H_9O_2{}^{i_2}$	$\frac{d\theta_{C_4H_2O_2{}^{i_2}}}{dt} = r_{19}$

Table S12 Objective function value at steady-state solution and norm of the difference between the steady-state solution and the 24 h solution

Temperature (K)	Objective function value	Distance to steady-state, d^{ss}
523	2.97E-06	4.22E-28
548	4.06E-05	2.88E-26
573	2.46E-07	1.14E-24
598	2.38E-12	5.19E-33
623	1.02E-05	1.33E-24
648	1.19E-09	5.91E-30
673	1.12E-08	1.32E-27
698	5.34E-08	2.49E-26
723	7.47E-08	5.71E-26
748	6.08E-08	3.55E-27
773	1.40E-12	1.43E-38
798	5.64E-12	5.07E-33
823	1.58E-04	2.45E-26
848	2.61E-06	9.51E-28
873	4.15E-05	1.92E-27
898	7.93E-04	2.40E-26
923	3.47E-10	1.19E-33

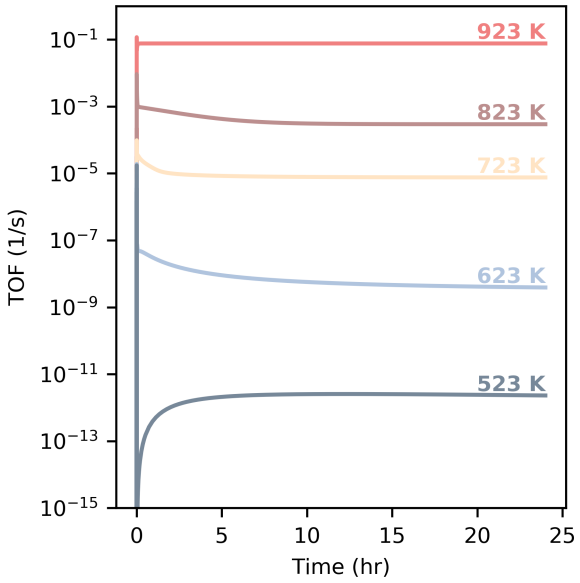

Fig. S12 Transient butadiene TOF for temperatures in the range 523 K–923 K for 24 h. The partial pressures of ethanol, hydrogen, and ethylene were 2 kPa, 0.02 kPa and 0.02 kPa, respectively, with trace amounts (2×10^{-8} kPa) of other gases, and a total pressure of 101.3 kPa.

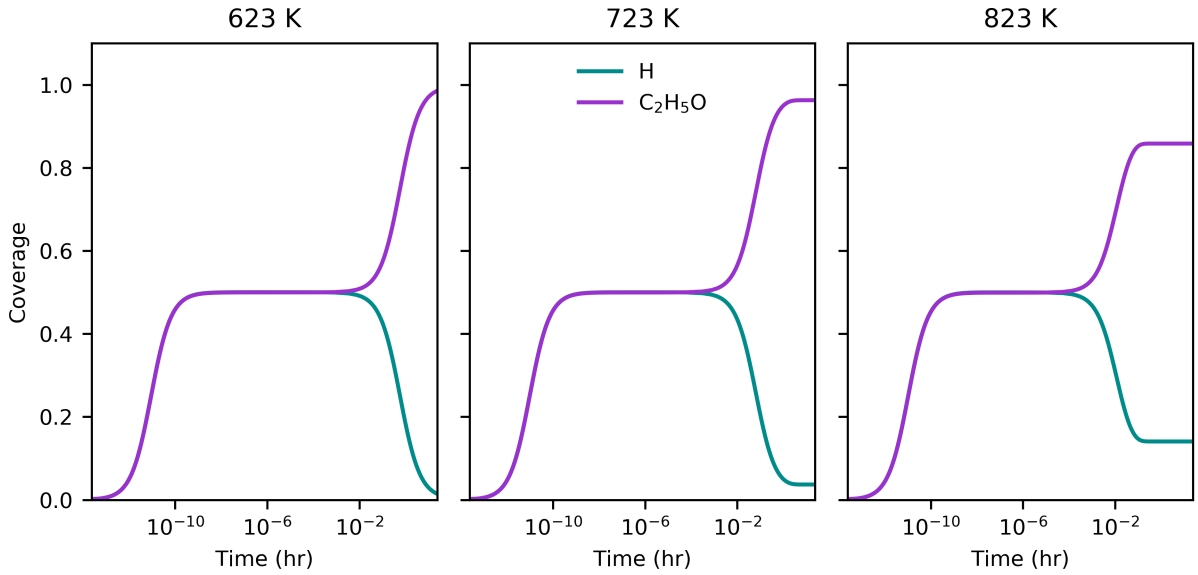

Fig. S13 Transient surface coverage of dominant species (coverage greater than 2%) in pathway p123. The partial pressures of ethanol, hydrogen and ethylene were $2\,\mathrm{kPa}$, $0.02\,\mathrm{kPa}$ and $0.02\,\mathrm{kPa}$ respectively with trace amounts ($2 \times 10^{-8}\,\mathrm{kPa}$) of other gases, and a total pressure of $101.3\,\mathrm{kPa}$.

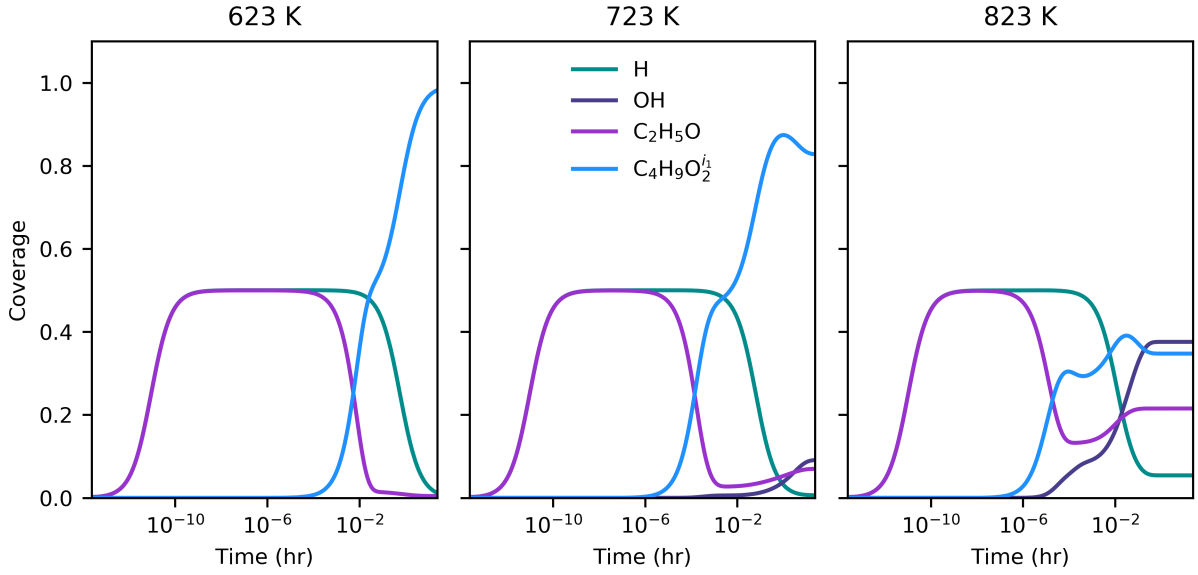

Fig. S14 Transient surface coverage of dominant species (coverage greater than 2%) in pathway p124. The partial pressures of ethanol, hydrogen and ethylene were $2\,\mathrm{kPa}$, $0.02\,\mathrm{kPa}$ and $0.02\,\mathrm{kPa}$ respectively with trace amounts ($2 \times 10^{-8}\,\mathrm{kPa}$) of other gases, and a total pressure of $101.3\,\mathrm{kPa}$.

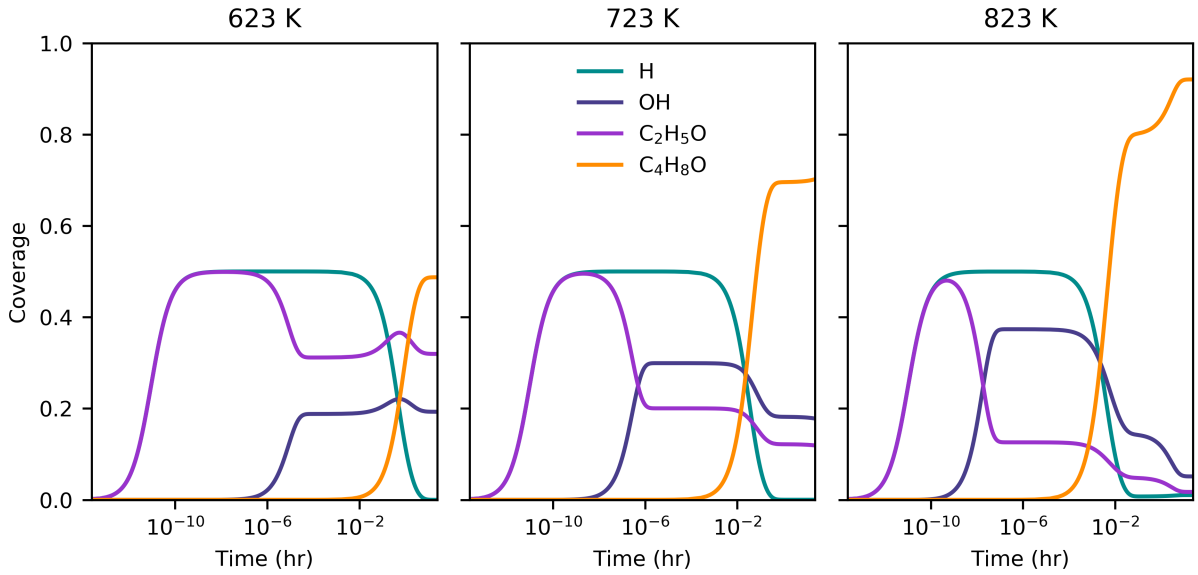

Fig. S15 Transient surface coverage of dominant species (coverage greater than 2%) in pathway p156. The partial pressures of ethanol, hydrogen, and ethylene were 2 kPa, 0.02 kPa and 0.02 kPa, respectively, with trace amounts (2×10^{-8} kPa) of other gases, and a total pressure of 101.3 kPa.

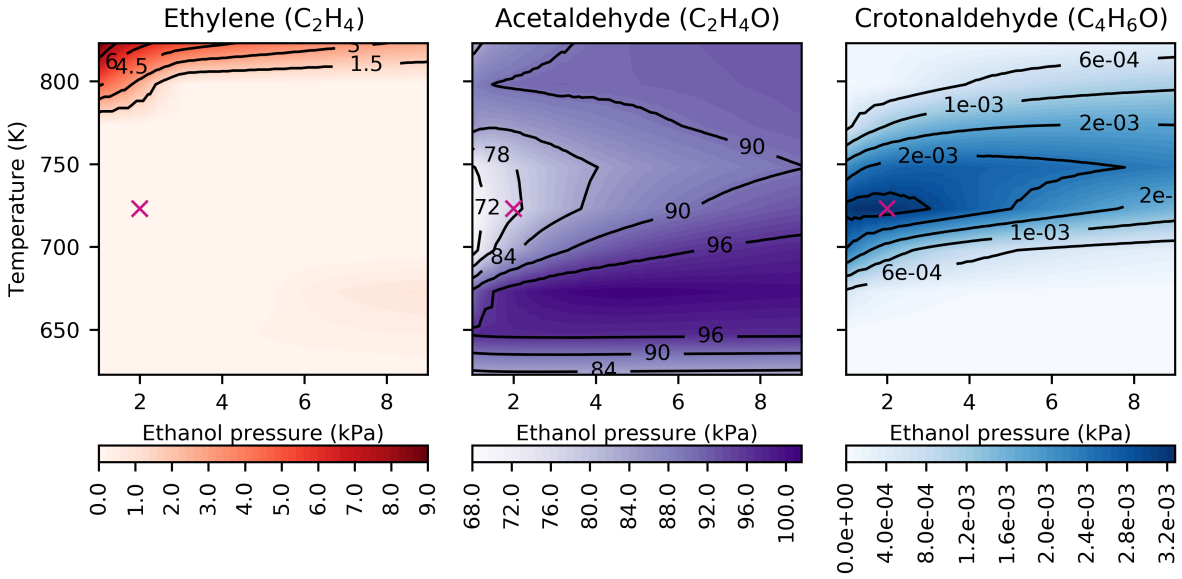

Fig. S16 Byproduct selectivity as a function of ethanol partial pressure and temperature after 24 h operation. Marker indicates conditions used in other results figures. The partial pressures of hydrogen and ethylene were 0.02 kPa with trace amounts (2×10^{-8} kPa) of other gases, and a total pressure of 101.3 kPa.

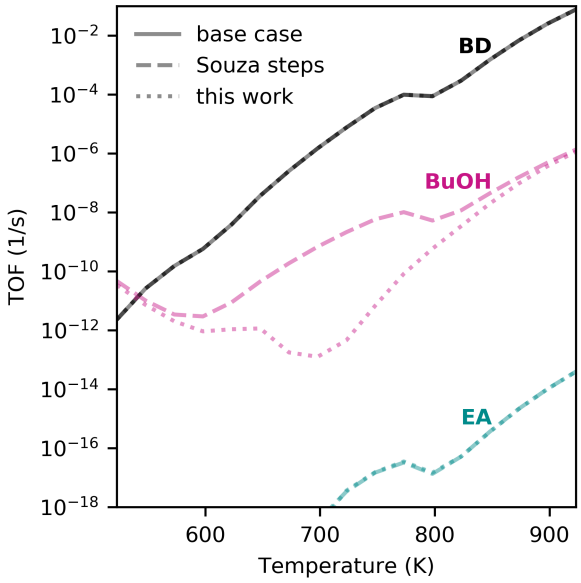

Fig. S17 Byproduct production rates as a function of temperature after 24 h operation. Solid lines show base case microkinetic model (Table S9), broken lines show microkinetic model with additional steps for butanol (BuOH) and ethyl acetate (EA) formation (Table S10). Butanol steps from Souza *et al.*[10] and this work are compared with the dashed and dotted lines respectively, in both cases including ethyl acetate steps from this work. The partial pressures of ethanol, hydrogen, and ethylene were 2 kPa, 0.02 kPa and 0.02 kPa, respectively, with trace amounts (2×10^{-8} kPa) of other gases, no butanol and ethyl acetate, and a total pressure of 101.3 kPa.

8 Impact of uncertainty

We assessed the impact of uncertainty in the free energy landscape on the predicted kinetics of the energy span and microkinetic models using a correlated error model, as described in the main text. The same 100 noisy samples of the reaction free energies were used for both models. The TOFs predicted by the energy span model for each pathway with the noisy samples are compared to the original, noise-free prediction in Figs. S18–S20, and the noisy and base case TOF predictions of the full microkinetic model are compared in Fig. S21. The individual samples obtained with both models span a fairly wide range of values; however, the mean values are similar in most cases. The broad span is to be expected considering that the energies occur in the exponent in the rate calculations; thus, a small perturbation to a barrier can result in a large modification of the corresponding rate. The trends noted in the main text were preserved: p123 is more active than p124 and p156 is least active, and the microkinetic model predicts a lower TOF than the theoretical upper bound on any pathway, on average. The rate control contributions (X_{TOF}) predicted by the energy span model for each pathway using the noisy samples are compared to the original, noise-free predictions for intermediate states in Fig. S22 and for transition states in Fig. S23. Again, the range of predictions is quite broad. Although the average predictions are mostly in agreement with the original data, different rate determining transition states are obtained in two cases (p156 at 623 K and 723 K) and there is greater contribution from multiple states in several cases (e.g. p124 at 723 K).

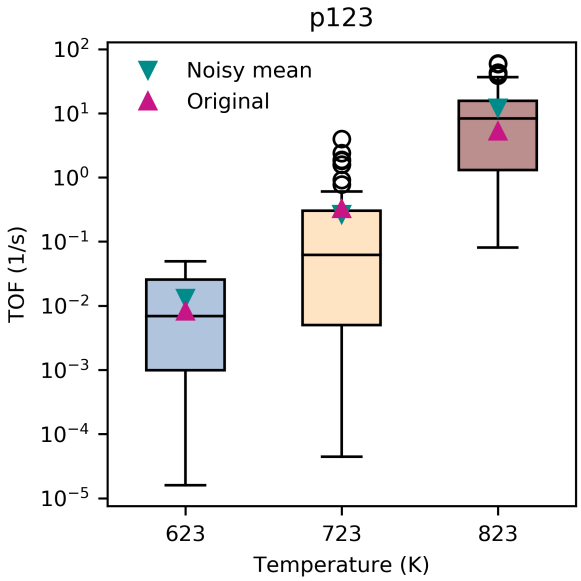

Fig. S18 Impact of perturbing the free energy landscape of p123 on the TOF predicted by the energy span model. Box-whisker plots were drawn from 100 samples. The box reflects the lower to upper quartiles with the median shown as a horizontal line. The whiskers reflect the range and the circles the outliers. Pink triangular markers give the raw, noise-free predictions and cyan markers give the mean of the noisy samples.

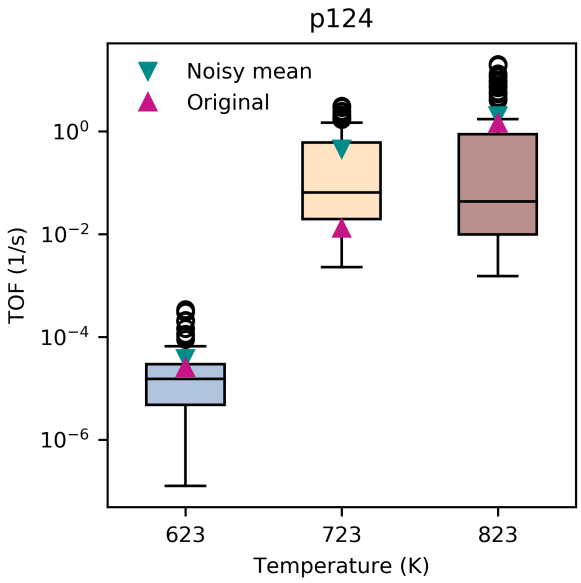

Fig. S19 Impact of perturbing the free energy landscape of p124 on the TOF predicted by the energy span model. Box-whisker plots were drawn from 100 samples. The box reflects the lower to upper quartiles with the median shown as a horizontal line. The whiskers reflect the range and the circles the outliers. Pink triangular markers give the raw, noise-free predictions and cyan markers give the mean of the noisy samples.

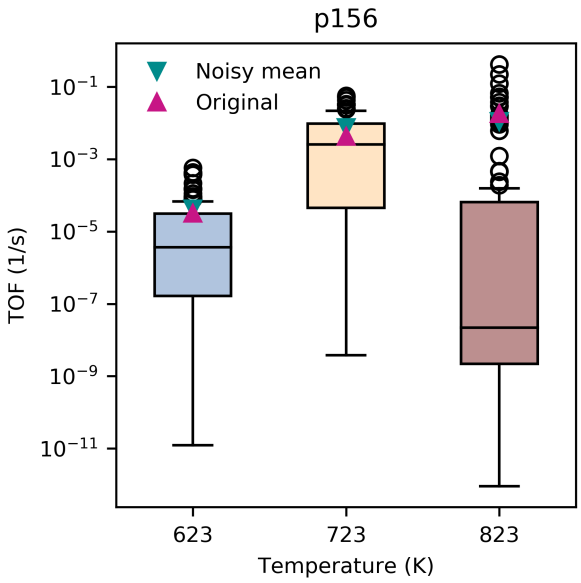

Fig. S20 Impact of perturbing the free energy landscape of p156 on the TOF predicted by the energy span model. Box-whisker plots were drawn from 100 samples. The box reflects the lower to upper quartiles with the median shown as a horizontal line. The whiskers reflect the range and the circles the outliers. Pink triangular markers give the raw, noise-free predictions and cyan markers give the mean of the noisy samples.

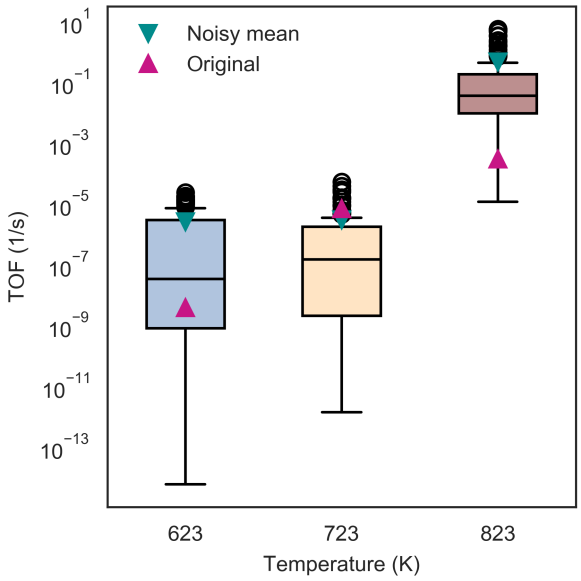

Fig. S21 Impact of perturbing the free energies of all states on the TOF predicted by the full microkinetic model. Box-whisker plots were drawn from 100 samples. The box reflects the lower to upper quartiles with the median shown as a horizontal line. The whiskers reflect the range and the circles the outliers. Pink triangular markers give the raw, noise-free predictions and cyan markers give the mean of the noisy samples.

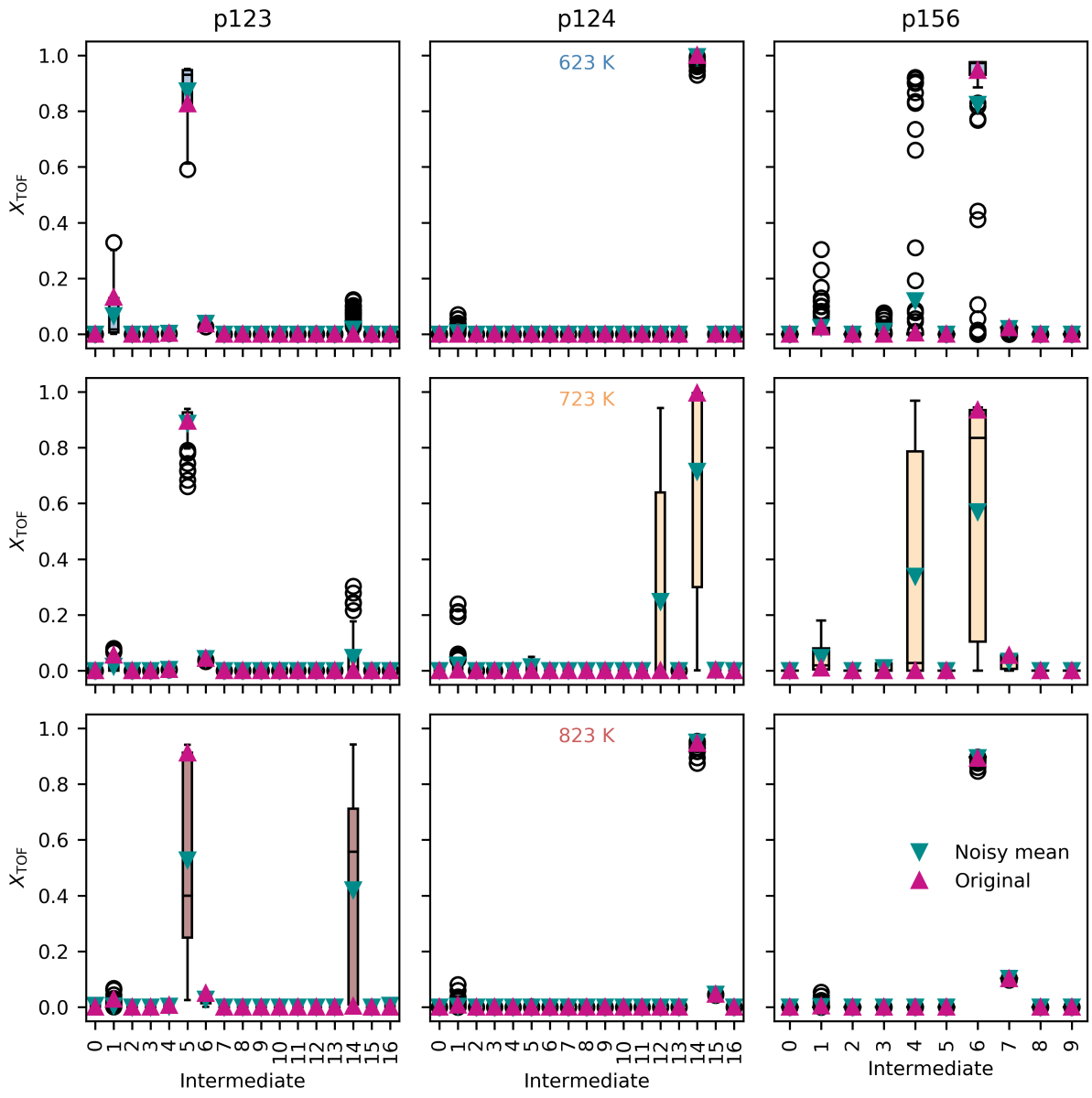

Fig. S22 Impact of perturbing the free energy landscape of each pathway on the rate contributions of each intermediate state predicted by the energy span model. Box-whisker plots were drawn from 100 samples. The box reflects the lower to upper quartiles with the median shown as a horizontal line. The whiskers reflect the range and the circles the outliers. Pink triangular markers give the raw, noise-free predictions and cyan markers give the mean of the noisy samples.

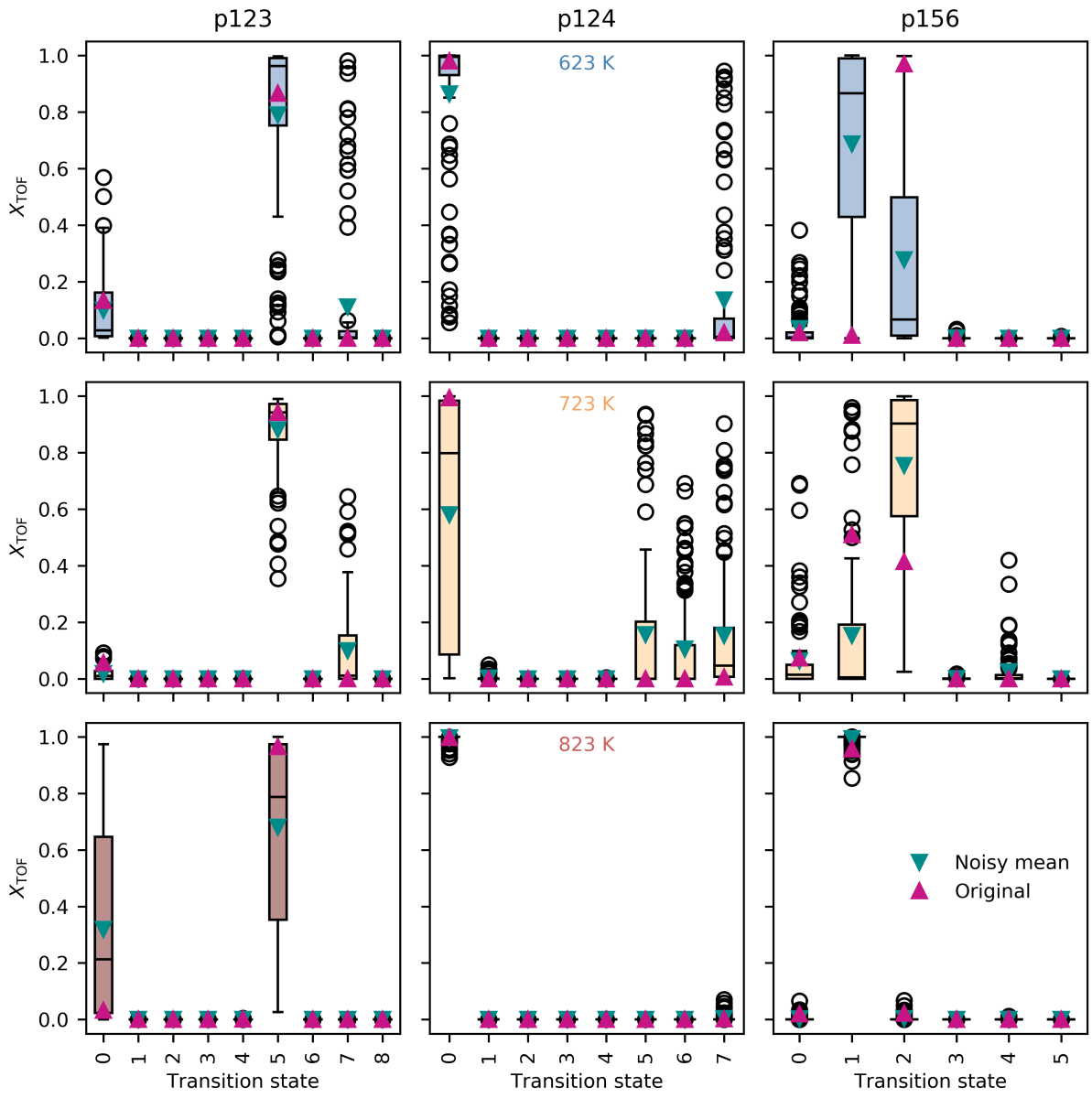

Fig. S23 Impact of perturbing the free energy landscape of each pathway on the rate contributions of each transition state predicted by the energy span model. Box-whisker plots were drawn from 100 samples. The box reflects the lower to upper quartiles with the median shown as a horizontal line. The whiskers reflect the range and the circles the outliers. Pink triangular markers give the raw, noise-free predictions and cyan markers give the mean of the noisy samples.

References

1 W. E. Taifan, T. Bučko and J. Baltrusaitis, *Journal of Catalysis*, 2017, **346**, 78–91.

2 F. Jensen, *Introduction to Computational Chemistry*, John Wiley & Sons, 3rd edn, 2017.

3 S. Kozuch and S. Shaik, *Accounts of Chemical Research*, 2011, **44**, 101–110.

4 A. Boje, *PyCatKin*, `https://github.com/aab64/PyCatKin`, 2021.

5 P. Virtanen, R. Gommers, T. E. Oliphant, M. Haberland, T. Reddy, D. Cournapeau, E. Burovski, P. Peterson, W. Weckesser, J. Bright, S. J. van der Walt, M. Brett, J. Wilson, K. J. Millman, N. Mayorov, A. R. J. Nelson, E. Jones, R. Kern, E. Larson, C. J. Carey, İ. Polat, Y. Feng, E. W. Moore, J. VanderPlas, D. Laxalde, J. Perktold, R. Cimrman, I. Henriksen, E. A. Quintero, C. R. Harris, A. M. Archibald, A. H. Ribeiro, F. Pedregosa, P. van Mulbregt and SciPy 1.0 Contributors, *Nature Methods*, 2020, **17**, 261–272.

6 C. Voglis and I. Lagaris, WSEAS International Conference on Applied Mathematics, 2004.

7 T. W. Birky, J. T. Kozlowski and R. J. Davis, *Journal of Catalysis*, 2013, **298**, 130–137.

8 S. Hanspal, Z. D. Young, H. Shou and R. J. Davis, *ACS Catalysis*, 2015, **5**, 1737–1746.

9 A. Chieregato, J. Velasquez Ochoa, C. Bandinelli, G. Fornasari, F. Cavani and M. Mella, *ChemSusChem*, 2015, **8**, 377–388.

10 E. F. de Souza, H. P. Pacheco, N. Miyake, R. J. Davis and F. S. Toniolo, *ACS Catalysis*, 2020, **10**, 15162–15177.